Plasma Sources Science and Technology

PAPER

Multiphysics simulation of the initial stage of plasma discharge formation in liquids

To cite this article: Ali Charchi Aghdam and Tanvir Farouk 2020 *Plasma Sources Sci. Technol.* **29** 025011

IOP Publishing Plasma Sources Science and Technology

Plasma Sources Sci. Technol. **29** (2020) 025011 (16pp) https://doi.org/10.1088/1361-6595/ab51e3

Multiphysics simulation of the initial stage of plasma discharge formation in liquids

Ali Charchi Aghdam and Tanvir Farouk[1]

Department of Mechanical Engineering, University of South Carolina, Columbia, SC 29208, United States of America

E-mail: tfarouk@sc.edu

Received 18 August 2019, revised 18 October 2019
Accepted for publication 28 October 2019
Published 11 February 2020

Abstract

Plasma initiation simulations in homogenous liquids in response to ~3.0–5.0 ns voltage pulse is conducted. An in-house numerical framework consisting of a compressible fluid solver together with charged species conservation and Poisson's equation solver is employed for the simulations. The simulations are conducted for a needle-like powered electrode with two different voltage profiles—linear and exponential increase. The model predictions show that under the influence of nanosecond voltage rise the liquid experiences the formation of negative pressure region near the vicinity of the powered electrode and surpasses the cavitation threshold pressure. The cavitation locations initiate as sub-micron regions and then extends up to a few microns. The electrical forces which is a combination of electrostatic, polarization and electrostrictive ponderomotive forces contributes significantly in cavitating the medium and forming low-density region. The ponderomotive forces have the highest impact followed by the polarization forces. The effect of electrostatic forces only become significant when sufficient free charges are formed. Despite the formation of low-density region, the ionization process is still predominantly driven by field dependent ionization—Zener tunneling; as the electric field across the sub-micron to micron scale low-density regions are not sufficient for electron impact ionization to be significant. A parametric study on maximum driving voltage and voltage profile is conducted. The results indicate that at higher voltage both the exponential and linear voltage profile form a compression wave and an associated high-density region in the medium. The magnitude of the compressive waves is not representative of shock waves. The bulk liquid velocity can reach hundreds of meters per second but maintains subsonic conditions when the maximum driving voltage is increased by a factor of 2.5–15 kV suggesting shock like conditions will be formed under higher electric field conditions.

Keywords: plasma in liquid, cavitation, field ionization, compression wave, electrical forces, field dependent ionization

1. Introduction

The topic of high-voltage interactions in liquid medium has been of interest amongst the scientific community in the past. There has been a resurgence in the interest in this topic in recent years as a result of studies related to plasma formation and interaction in liquid and multiphase configurations. The renewed research thrust and the exponential growth in liquid/multiphase plasma has been predominantly driven by their application in biological, biomedical and environmental application as evident in most of the review papers [1–5]. One of the earliest work in liquid phase plasma was conducted by Dawkins and Berg [6] reporting corona discharges in oils. Luminous spots were observed near submerged electrodes, hypothesized to be a result of localized field emission. Similar luminescence have been observed for pulsed electrode fields applied in liquid hexane [7, 8]. Liquid hydrocarbons were a first choice of these studies since the breakdown process in non-polar medium is less complex. Two mechanisms are generally highlighted for the electrical breakdown in liquids;

---

[1] Author to whom any correspondence should be addressed.

an electron-multiplication in the liquid phase and breakdown associated with pre-existing bubbles [9]. The formation of low-density region as a result of pre-existing bubble or phase change process can act as localized micro sources of discharges by reducing the breakdown electric field requirement. Discharges in gas bubbles in liquids have been extensively investigated experimentally in terms of the ability of bubbles and their chemical composition to modify gross plasma features. Bubble experiments with nitrogen, oxygen, and noble gases [10–14] in various fluids revealed similar behaviors under discharge excitation, with plasmas appearing primarily within the bubbles, but requiring different voltage amplitude for plasma initiation. The effects of discharge frequency on plasma formation and properties were also revealed, but not entirely characterized. Similarly, modeling studies have been devoted toward yielding fundamental insights on plasma formation, primarily for liquid media without the presence of bubbles [15]. Recent models have considered the presence of a single stationary bubble [16] within a liquid media and one-way coupling of the plasma discharge between the bubble and plasma to simulate experiments [17, 18]. Other similar single and multiple bubble scenarios have appeared to further characterize plasma initiation phenomena [19].

The formation and presence of vapor phase bubbles for the generation of non-thermal plasmas discharge in the liquid phase has been a topic of contention and a major unresolved issue is the formation and propagation of the very first vapor phase bubble that facilitates the primary streamer development [12]. Among the different theories, Lewis [20, 21] proposed that the liquid phase cracks under high dielectrophoretic stresses leaving a void due to electric fields and space charges to form bubbles. Joshi *et al* [19] suggested bubble formation from vaporization of the liquid as a result of heating effect. A theoretical study was conducted by Shneider *et al* [22] to determine the initiating mechanism of the sub-nanosecond pulsed breakdown in liquid dielectrics. It was proposed that the electrostrictive forces near the cathode could result in a rupture in the continuity of the fluid forming nanopores hence acting as plasma initiation sites. In a follow up study, they employed the Zeldovich–Fisher theory to determine the pre-breakdown nanopore formation due to cavitation process [23].

In this work a mathematical model has been developed to simulate plasma discharge formation in liquid water. The kinetic steps considered are, ionization, recombination and attachment processes. The primary objective of this study is to computationally investigate the plasma initiation process in the liquid phase in the nano-second time scales and the associated density variation of the medium due to the electric field, charges and the associated forces. We investigate two different voltage driving conditions, a linear ramp and an exponential ramp. The role of the different force terms on density variation was elucidated, including the time dependent evolution of the charged species and electric field. The impact of the ionization process through Zener tunneling was also independently studied.

2. Mathematical model

The mathematical model proposed consists of the fluid dynamic equations of the mass, momentum and energy conservation for the bulk medium in compressible form, species conservation equations for each of the species considered (electrons n_e, positive ions n_p and negative ions n_n) and the Poisson's equation for the electric field. A local field approximation is employed to determine the electron temperature as a function of the reduced electric field ($|\mathbf{E}|/N$).

2.1. Governing equations

The mass, momentum and energy conservation of a compressible Newtonian fluid is described by the following equations:

$$\frac{\partial \rho}{\partial t} + \nabla.(\rho \mathbf{U}) = 0 \tag{1}$$

$$\frac{\partial \rho \mathbf{U}}{\partial t} + \nabla.(\rho \mathbf{U}.\mathbf{U}) = \mu \nabla^2 \mathbf{U} - \nabla p + \mathbf{F} \tag{2}$$

$$\begin{aligned}\frac{\partial \rho E_{\text{tot}}}{\partial \text{t}} &+ \nabla \cdot (\rho \mathbf{U} E_{\text{tot}}) + \nabla \cdot (\mathbf{U} p)\\ &= - \nabla \cdot \mathbf{q} + \nabla \cdot (\tau \cdot \mathbf{U}) + \mathbf{J}_{\text{ion}} \cdot \mathbf{E},\end{aligned} \tag{3}$$

where, ρ is the liquid density, $\mathbf{U}$ is the velocity vector, μ is the viscosity, p is the hydrodynamic pressure and $\mathbf{F}$ is the electrical force vector. In the energy conservation equation E_{tot} is the total energy, $\mathbf{q}$ is the conductive heat flux, τ is the viscous stress tensor and $\mathbf{J}_{\text{ion}}$ is the ion current density.

The electrical force vector $\mathbf{F}$ contains three terms and has the following form:

$$\mathbf{F} = q\mathbf{E} - \frac{\epsilon_0}{2}\mathbf{E}^2 \nabla \epsilon + \frac{\epsilon_0}{2} \nabla \left(\mathbf{E}^2 \frac{\partial \epsilon}{\partial \rho} \rho \right), \tag{4}$$

where, q is the charge density, ε_o is the vacuum dielectric permittivity, ε is the relative permittivity and $\mathbf{E}$ is the electric field vector. The first term in the right hand side of equation (4) is the electrostatic force i.e. the force acting on the free charges, the second term is the force associated with the non-uniformity of the permittivity and the third term is the force due to electric field gradient. The second and third terms are customarily termed as polarization and electrostrictive ponderomotive forces, respectively [24]. The term $\frac{\partial \varepsilon}{\partial \rho}$ is a fluid property. For polar dielectrics like water, it has been shown in [25] that at a constant temperature, the variation in permittivity as a function of density can be expressed in the following form:

$$\varepsilon = \varepsilon_l \left(\frac{\rho}{\rho_l} \right)^a, \tag{5}$$

where, ε_l is the relative permittivity of water at atmospheric pressure and room temperature and has a value of 80.79, ρ_l is the associated liquid density and a is constant having a value of 1.34 for water. The last term in equation (4) can be simplified for a polar liquid as suggested in [24]:

$$\frac{\partial \varepsilon}{\partial \rho}\rho = a\varepsilon. \tag{6}$$

The Tait equation of state [26] is often used to relate the pressure to the density of water.

$$p = (p_o + B)\left(\frac{\rho}{\rho_o}\right)^{\gamma} - B \tag{7}$$

here, $\rho_o = 1000\ \mathrm{kg\ m^{-3}}$, $p_o = 10^5$ Pa, $B = 3.5 \times 10^5$ Pa and $\gamma = 7.5$. However, to simplify the pressure-momentum coupling, instead of the Tait equation a linear sonic compressibility model is used:

$$\rho = \rho_o + \psi p. \tag{8}$$

The symbol ψ is referred to as the compressibility of the medium and is defined as:

$$\psi = \left(\frac{\partial \rho}{\partial p}\right)_s. \tag{9}$$

The compressibility of a medium is directly related to the speed of sound ($\psi = 1/c^2$). Assuming a constant speed of sound in water over the range of pressure of our interest, the compressibility of water is found to have a value of $\psi = 4.54 \times 10^{-7}\ \mathrm{s^2\ m^{-2}}$, obtained from linear regression of the Tait expression over a pressure range of ± 100 MPa. As mentioned in [27], the deviation between acoustic and Tait equation of state in the aforementioned range is not more than 1%. The pressure gradient term in equation (2) can then be expressed in terms of a density gradient $\nabla p = \frac{1}{\psi}\nabla \rho$.

The total pressure acting on the fluid is the sum of thermodynamic pressure and the pressure associated with the electrical force (equation (4)), which we refer to as electrical pressure $-\nabla(p_E) = \mathbf{F}$. If the electrical pressure only had contribution from ponderomotive forces, the expression could be analytically integrated to obtain the expression for the electrical pressure. However, since the contribution of electrostatic and polarization forces are also being considered, the electrical pressure term is integrated numerically. For convenience, the numerical integration is performed by converting the electrical pressure expression into an elliptic partial differential equation through divergence operation. The equation being solved has the following form:

$$\nabla.(\nabla p_E) = -\nabla\ .\ \mathbf{F}. \tag{10}$$

The species transport equation employed is as follows:

$$\frac{\partial n_k}{\partial t} + \nabla.(n_k \mathbf{U}) + \nabla.(\pm\mu_k \mathbf{E} n_k) = \nabla.(D_k \nabla n_k) + \dot{n}_k, \tag{11}$$

where, n_k is the number density of kth species and k = electrons (e), positive (p) and negative (n) ions, μ_k and D_k is the mobility and the diffusion coefficient for kth species respectively and $\dot{n}_k$ is the source term. The second term in equation (11) represents the flux of species due to the bulk fluid motion.

Cross section data of elastic scattering, electron impact ionization and electron attachment were obtained from Itikawa and Mason [28] to generate the electron transport properties and reaction rates over a range of reduced electric field ($|\mathbf{E}|/N$) by BOLSIG+ [29]. As an approximation, the liquid media is assumed to be a dense gas with high particle number density [30] and the electron transport properties are evaluated at the corresponding $|\mathbf{E}|/N$ values for such gas. For the positive and negative ions, mobility values of $\mu_p = 3.5 \times 10^{-7}\ \mathrm{m^2\ V^{-1}\ s^{-1}}$, $\mu_n = 2.0 \times 10^{-7}\ \mathrm{m^2\ V^{-1}\ s^{-1}}$ from [31] and diffusivity values of $D_{k=p,n} = 10^{-9}\ \mathrm{m^2\ s^{-1}}$ from [5] were used.

Source terms in the species transport equations are determined based on chemical reaction rates of the kinetic processes. The source terms for the electrons, positive and negative ions are expressed as follows:

$$\dot{n}_e = Z_I + k_{\mathrm{ion}} n_e n_{\mathrm{neut}} - k_{\mathrm{attach}} n_e n_{\mathrm{neut}} - k_{\mathrm{recomb1}} n_e n_p \tag{12}$$

$$\dot{n}_p = Z_I + k_{\mathrm{ion}} n_e n_{\mathrm{neut}} - k_{\mathrm{recomb2}} n_p n_n - k_{\mathrm{recomb1}} n_e n_p \tag{13}$$

$$\dot{n}_n = k_{\mathrm{attach}} n_e n_{\mathrm{neut}} - k_{\mathrm{recomb}} n_p n_n. \tag{14}$$

The kinetic processes considered are field dependent ionization (Z_I), electron impact ionization (k_{ion}), electron attachment (k_{attach}), electron–ion recombination (k_{recomb1}) and ion–ion recombination (k_{recomb2}). For the kinetic processes till now it is common practice to consider the liquid as a dense medium for qualitative description of the phenomena since there is no definitive theoretical understanding/interpretation of the ongoing kinetic processes [30]. We consider both electron impact ionization and electron tunneling processes and assume that the overall ionization occurs as a combination of both. Due to the very small-time scale and the associated small mean free path of liquids the avalanche ionization seems to be less likely for the conditions of interest.

The attachment and ionization coefficients are tabulated as lookup tables for a range of reduced electric field ($|\mathbf{E}|/N$). For the electron–ion (k_{recomb1}) and ion–ion (k_{recomb2}) recombination a constant rate constant of $10^{-19}\ \mathrm{m^3\ s^{-1}}$ is used, similar to the work of Qian *et al* [31]. The field dependent ionization rate which corresponds to ionization due to Zener tunneling for water has been adopted from [31] and is expressed as:

$$Z_I(\mathbf{E}) = \beta n_{\mathrm{neut}} \frac{q|\mathbf{E}|d}{h} \exp\left(-\frac{m_e d \pi^2 \Delta^2}{q|\mathbf{E}|h^2}\right), \tag{15}$$

where, β is the fraction of ionizable species, n_{neut} is the number density of neutral species obtained from the density of the fluid, d is the molecular separation distance (0.31 nm for water), h is the Planck's constant, m_e is the effective electron mass and Δ is the ionization energy barrier for water. An ionization energy barrier of 4 eV [32, 33] is employed.

The electric field is obtained from the Poisson's equation and expressed in the following form:

$$-\nabla.\varepsilon\nabla\phi = \frac{e}{\varepsilon_o}(n_p - n_n - n_e), \tag{16}$$

where, ϕ is the electric potential and e is the electron charge.

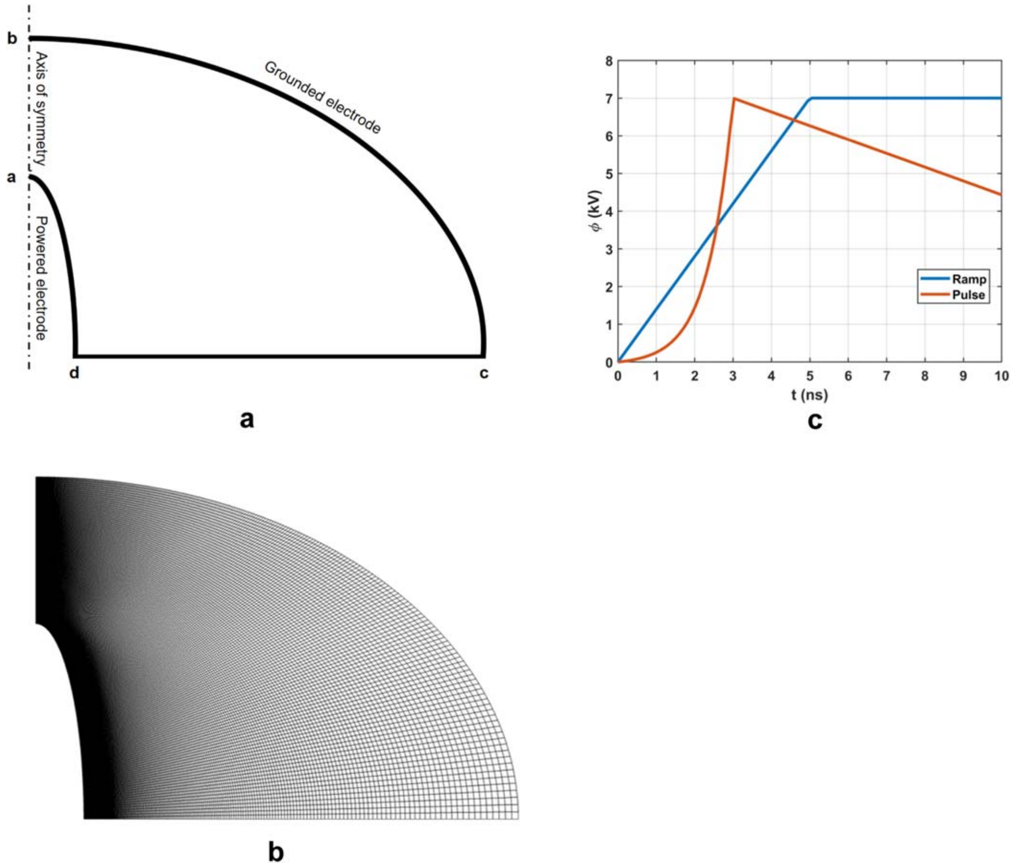

Figure 1. (a) Schematic of the problem geometry, (b) computational mesh considered in the present study and (c) two different voltage profile employed at the powered electrode.

2.2. Boundary conditions

Standard no-slip and zero gradient boundary conditions were utilized for velocity and density respectively at all the boundaries. For energy equation, adiabatic wall boundary condition was prescribed. The electric potential at the grounded electrode is set to zero and a time varying potential representative of nano-second pulse is prescribed at the powered electrode.

Flux boundary conditions were used for species at the electrodes. The flux of electrons and ions at the electrode walls are given as:

$$\mathbf{\Gamma}_e = \frac{1}{4} n_e u_{\mathrm{th}} - \gamma_{\mathrm{se}} \sum_i q_i \mathbf{\Gamma}_i \tag{17}$$

$$\mathbf{\Gamma}_i = \frac{1}{4} n_i u_{\mathrm{th},i} + b \mu_i \mathbf{E} n_i, \tag{18}$$

where u_{th} is the thermal velocity and γ_{se} is the secondary electron emission coefficient having a value of 0.01 and q is the sign of the ion charge. In equation (18), $b = 0$ for the powered electrode and $b = 1.0$ for the grounded electrode. All the other boundaries are treated as zero-flux boundaries for all species.

A boundary condition is required for the electric pressure (equation (10)). Since ε is a function of liquid density only and as already noted, $\nabla \rho = 0$ at all the boundaries, the polarization force is zero in all the boundaries. Assuming the electrostatic forces to be negligible at the boundaries and ponderomotive forces being prominent, the following boundary condition for electric pressure is obtained:

$$p_E = \frac{\varepsilon_0}{2} a \varepsilon \mathbf{E}^2. \tag{19}$$

2.3. Numerical scheme

The numerical scheme for solving the governing equations is based on the finite volume approach. The sets of equations are assembled and solved in the OpenFOAM framework [34]. The discretized equations are solved in a sequential manner. The Poisson's equation is solved with a semi-implicit solver for the electric field which allows calculating the electric forces and obtaining the force terms for the momentum equations. The fluid velocity and the pressure are obtained by solving the coupled continuity and momentum equation together with the pressure-density state relation using Pressure-Implicit with Splitting Operators algorithm [35]. The individual species transport equation and the energy conservation equation is then solved. The pressure interpolation for the collocated grid is performed following the Rhie and Chow scheme [36]. First-order implicit Euler scheme is used for time integration of all the partial differential equations with a variable time stepping and the maximum time step size

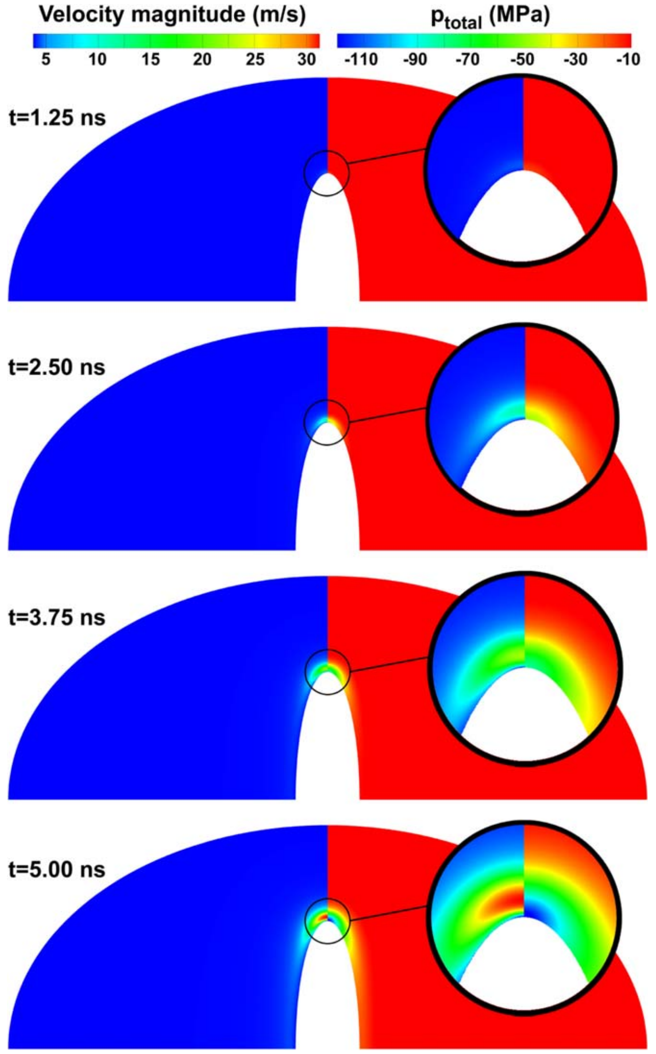

Figure 2. Spatio-temporal contour plots of velocity magnitude and total pressure for the linear ramp case ($V_{\max} = 7.0$ kV, $\beta = 1.0$). The inset shows a zoomed view very close to the electrode tip.

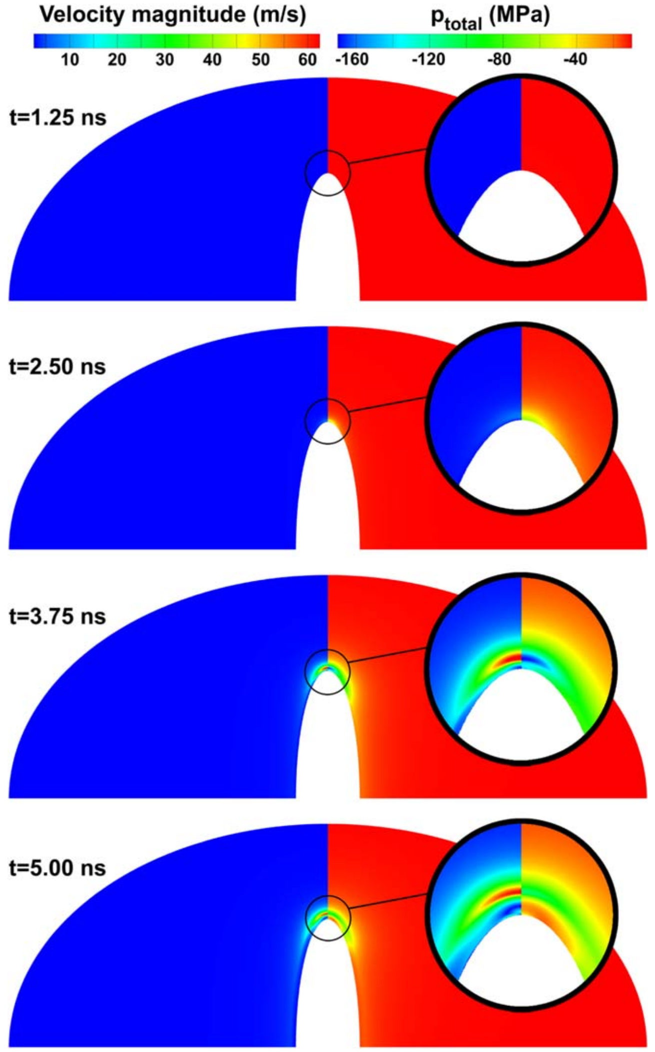

Figure 3. Spatio-temporal contour plots of velocity magnitude and total pressure for the pulse case ($V_{\max} = 7.0$ kV, $\beta = 1.0$). The inset shows a zoomed view very close to the electrode tip.

limited to 10^{-12} s. Divergence terms in momentum and species equations were treated with the flux-limited scheme and linear interpolation with orthogonal correction was used for discretizing the Laplacian terms. Species source terms were included in the species conservation equations using OpenFOAM's implicit/explicit source switching feature. This feature automatically switches between an implicit and explicit mode for source term to ensure the diagonal dominance of the matrix. The discretized momentum, pressure, energy and species equations are solved using stabilized preconditioned conjugate gradient solver with diagonal incomplete LU preconditioner. Poisson's equation is solved by Geometric-algebraic multi-grid solver. Iterations are done until a desired residual, of 10^{-8} for momentum and energy and 10^{-12} for pressure and electric potential is attained.

3. Problem geometry

Figure 1(a) depicts the computational domain for the liquid phase plasma discharge simulations. The discharge is initiated with a needle like electrode that is powered. Due to symmetry, only half of the geometry is simulated. The line a-b is the axis of symmetry. The boundary a-d denotes the powered electrode. The boundary b-c is the grounded electrode. The smallest distance between the powered and grounded electrode is 60 μm (a-b). The length of c-d is chosen to be 180 μm along which zero gradient boundary conditions are prescribed. A structured non-uniform mesh of 89 000 cells was employed with denser grids present near the powered electrode and shortest inter-electrode separation distance (figure 1(b)). The meshing operation is performed with the Gmsh package [37]. Two different pulse profiles were applied to the powered electrode (figure 1(c))—'linear ramp' $\left(V(t) = V_{\max}\left(\frac{t}{t_n}\right),\ t_n = 5 \times 10^{-9}\right)$ and 'rapid pulse' $(V(t) = c_1 V_{\max}(c_1^{-\frac{t}{\tau_1}} - 1)$ for $t < \tau_1$, $c_1 = 0.01$, $\tau_1 = 3 \times 10^{-9}$ and $V(t) = \left(\frac{V_{\max}}{2(\delta - \tau_2)}\right)t + \left(V_{\max} - \frac{V_{\max}\tau_1}{2(\delta - \tau_2)}\right)$ for $\tau_1 \leqslant t \leqslant \tau_2$, $\delta = \tau_1 - \tau_1\frac{\log(2c_1)}{\log(c_1)}$, $\tau_2 = 10 \times 10^{-9}\Big)$. In the 'linear ramp' case, the electrode was subject to a linearly ascending ramp and in the 'rapid pulse' case, the applied voltage

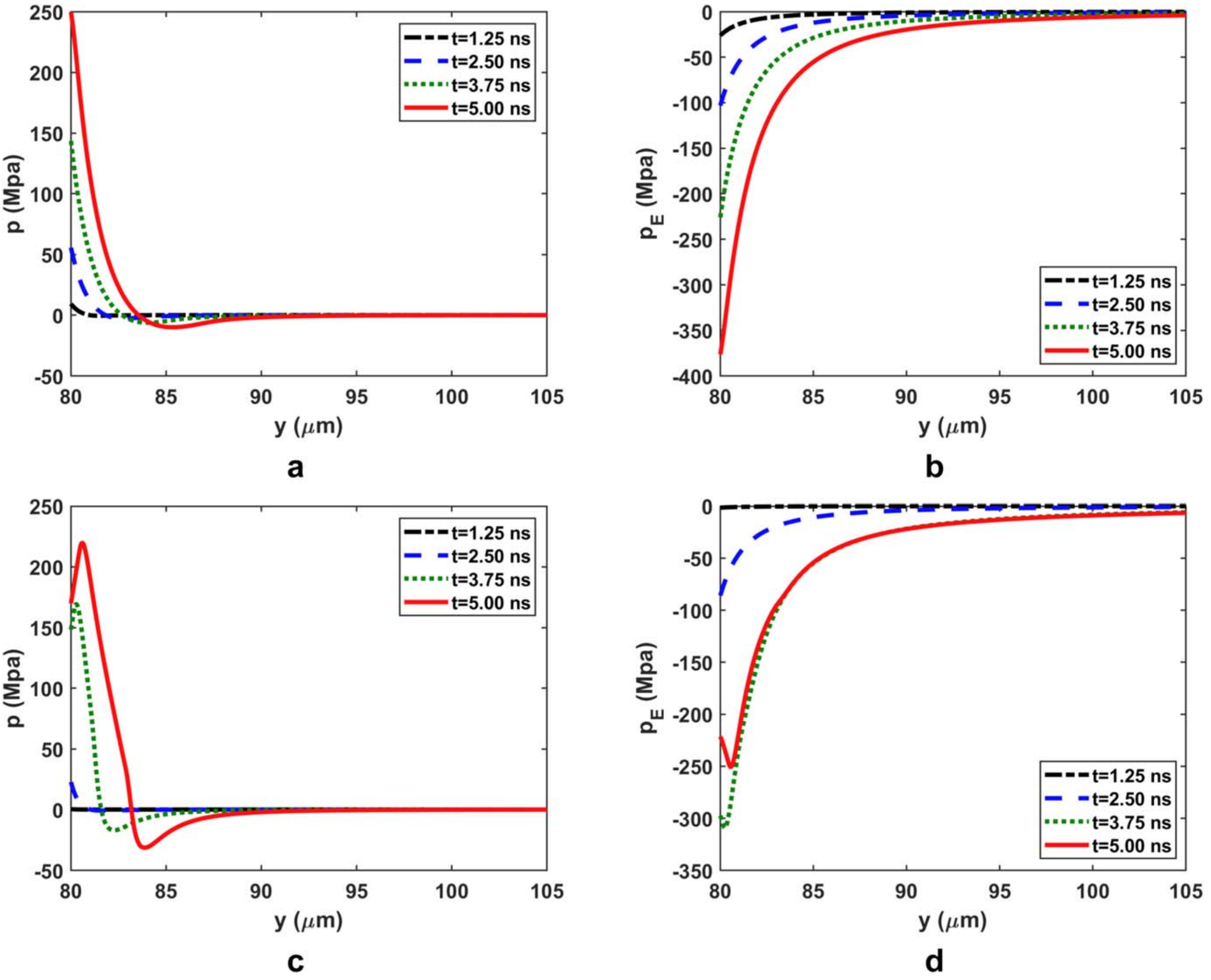

Figure 4. Center line distribution of hydrodynamic and electric pressure at different time instances for the linear ramp (a), (b) and pulsed case (c), (d). ($V_{\max} = 7.0\,\text{kV}$, $\beta = 1.0$.).

was increased exponentially. It should be noted that both profiles had identical maximum voltage of 7 kV. However, unlike the 'rapid pulse' case where the voltage starts to decrease once the peak voltage is attained, the maximum voltage is maintained for the 'linear ramp' case.

4. Results and discussions

Simulations have been conducted for plasma initiation in distilled water for a powered needle like electrode. The needle electrode is either exposed to a linear ramp or a pulsed profile as shown in figure 1(c). For the base case, the maximum voltage for both voltage profiles is 7 kV which was chosen to be consistent with the work of Shneider and Pekker [24]. Figures 2 and 3 show the spatial variation of the bulk fluid velocity magnitude and total pressure (i.e. $p_{\text{total}} = p + p_E$) in the domain at different points of time. For both the voltage profiles a negative pressure region near the electrode is progressively formed within 5 nanoseconds. The low-pressure region is formed as a result of the contributions from electrical forces. The magnitude of the negative pressure region for the two cases are not identical despite the identical maximum voltage value. For the pulse case the total pressure had a lowest value of ~ -180 MPa which was ~ -115 MPa for the linear ramp. Apart from the magnitude of the total pressure, a far more distinctive characteristics related to the low-pressure region is observed between the two cases. Under linear ramping, the low-pressure region remains stationary adjacent to the powered electrode. However, with a pulsed profile, a propagating low-pressure wave followed by a high-pressure region is seen. The time response of the hydrodynamic pressure has an initial buildup period. If the hydrodynamic pressure is of higher magnitude it can compensate any possible negative electric pressure contributions. For the pulse case, as the electric field strength decreases after the peak voltage the electric pressure starts to decrease however the hydrodynamic pressure continues to grow resulting in a propagating high-pressure wave. The resulting velocity magnitude for the two different driving voltage profile

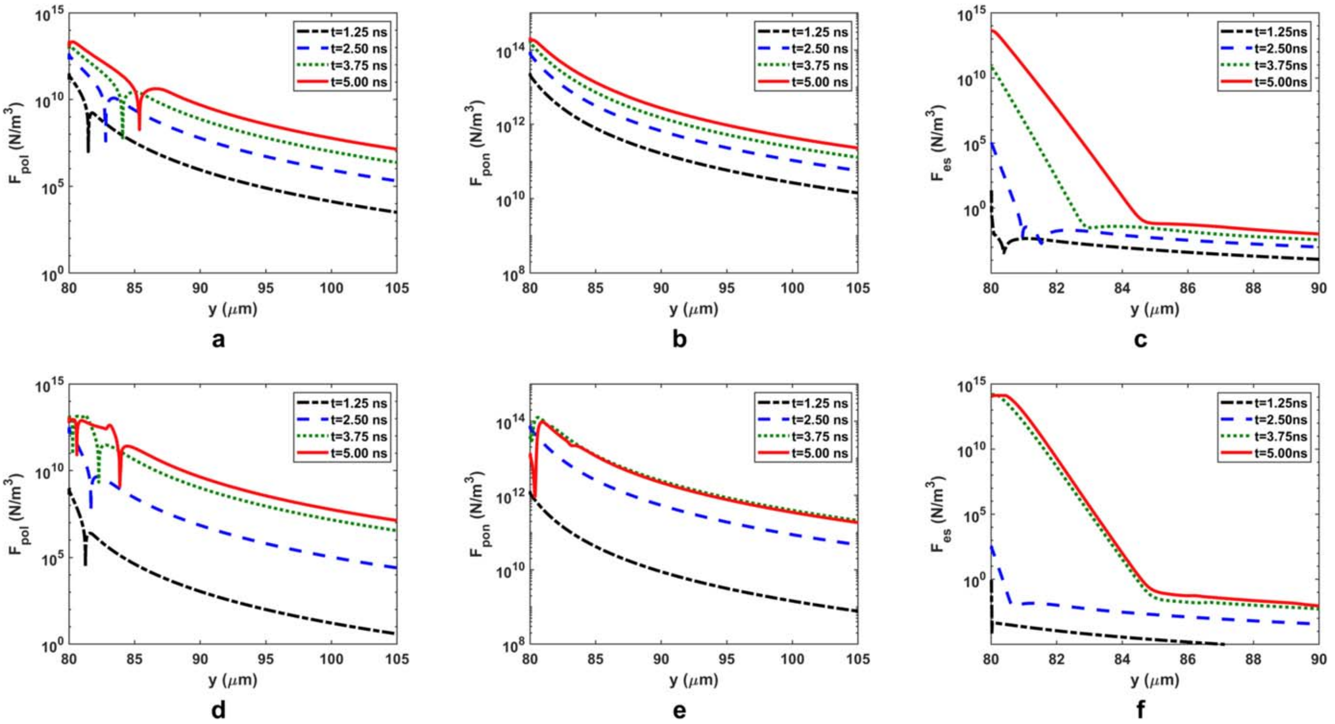

Figure 5. Spatial evolution of polarization (a), (d), ponderomotive (b), (e) and electrostatic (c), (f) forces along the center line at different time instances. Forces for the linear ramp case are presented in (a)–(c). Figures (d)–(f) represent pulsed case. ($V_{\max} = 7.0$ kV, $\beta = 1.0$.).

indicates the formation of a high velocity region near the powered electrode. The peak velocity magnitude is in the range of tens of meter per second; a subsonic flow condition. It should be noted though that the bulk fluid velocity of the domain is dictated by the peak value of the applied voltage as well the voltage profile. For the same peak voltage, a pulsed profile results in a peak velocity which is a factor of two higher than that of the linear ramp case. The resulting bulk fluid temperature is found to increase by ~1 K only (not shown here).

The center line distribution of hydrodynamic and electric pressure for the same linear ramp and pulsed case are presented in figure 4. For both the voltage profiles there is a buildup of the hydrodynamic pressure near the electrode surface. This high-pressure region is indicative of the bulk fluid undergoing compression. This region extends to ~4 μm from the electrode surface. The hydrodynamic pressure also undergoes a distinctive pressure reversal (i.e. formation of negative pressure region). For the linear ramp, where the magnitude of the negative hydrodynamic pressure is lower, the pressure reversal has a significantly lower gradient in comparison to the pulse case. Both these reversals occur at ~4 μm from the electrode surface and extends up to ~3 μm. On the other hand, the electric pressure having predominant contribution from the polarization and ponderomotive forces have very large negative pressure near the electrode. The electric pressure maintains very sharp gradients within ~5 μm and then asymptotically diminishes. The negative electric pressure region extends to almost ~20 μm when the maximum driving voltage is attained.

The distribution of the polarization ($\mathbf{F}_{\mathrm{pol}}$) and ponderomotive ($\mathbf{F}_{\mathrm{pon}}$) and electrostatic forces ($\mathbf{F}_{\mathrm{es}}$) along the centerline is presented in figure 5. It can be seen that the $\mathbf{F}_{\mathrm{pon}}$ which results from the electric field gradients, has the maximum contribution. On the other hand, the polarization force depends on the gradient of the dielectric permittivity which is a function of medium density. As a result, $\mathbf{F}_{\mathrm{pol}}$ is in effect only after a density gradient is established by the other forces. The strong dependence of the $\mathbf{F}_{\mathrm{pol}}$ on the density field leads to its slower response to voltage changes in the domain. Compared to $\mathbf{F}_{\mathrm{pon}}$, $\mathbf{F}_{\mathrm{pol}}$ force is effective in a smaller region range near the powered electrode surface. For both the ramp and pulse case, $\mathbf{F}_{\mathrm{pon}}$ is an order of magnitude higher than that of the $\mathbf{F}_{\mathrm{pol}}$. For the linear ramp case, $\mathbf{F}_{\mathrm{pon}}$ continues to increase while for a pulsed voltage it decreases once the driving voltage starts to decrease. Between the two cases a noticeable difference is seen in the $\mathbf{F}_{\mathrm{pol}}$ profile as well. A sharp increase in $\mathbf{F}_{\mathrm{pol}}$ is observed only for the pulse due to the propagating high pressure wave (figure 4(c)) and the associated increase in density. From the distribution of the different electrical forces it is evident that magnitude of $\mathbf{F}_{\mathrm{es}}$ is not comparable to either $\mathbf{F}_{\mathrm{pol}}$ and $\mathbf{F}_{\mathrm{pon}}$ initially. Once ionization takes place its magnitude is similar to that of $\mathbf{F}_{\mathrm{pol}}$ due to the presence of the charged species.

Figure 6 presents the transient evolution of the centerline profile of the fluid density and axial component of the velocity. The fluid density increases to its maximum in the vicinity of the electrode tip as a result of compressive stresses (figures 4(a), (c)). A small region of rarefaction spanning ~3 μm occurs due to the fluid motion and stretching under the influence of both polarization and pondermotive forces.

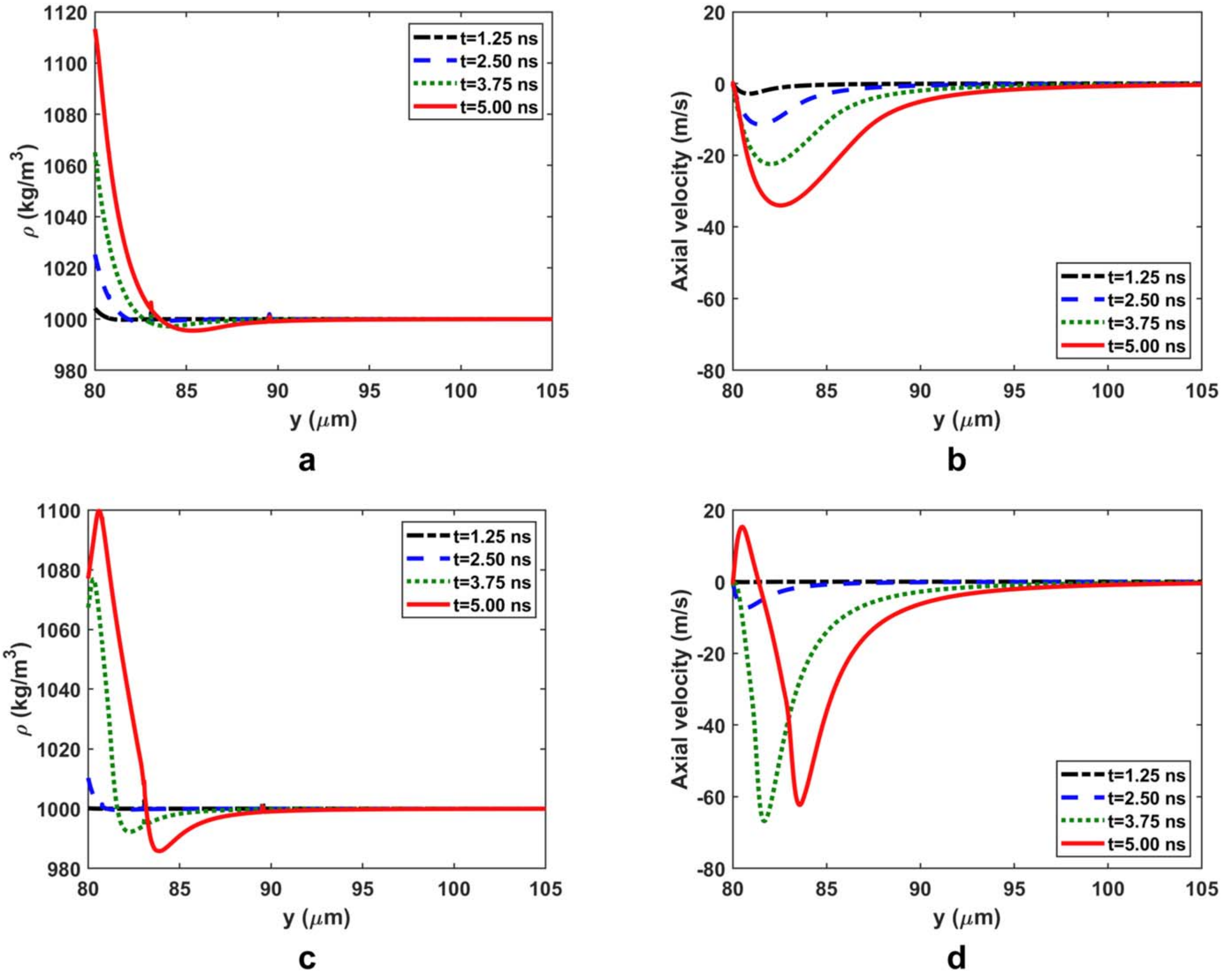

Figure 6. Center line distribution of fluid density and axial velocity at different time instances for the linear ramp (a), (b) and pulsed case (c), (d). ($V_{\max} = 7.0\,\text{kV}$, $\beta = 1.0$.).

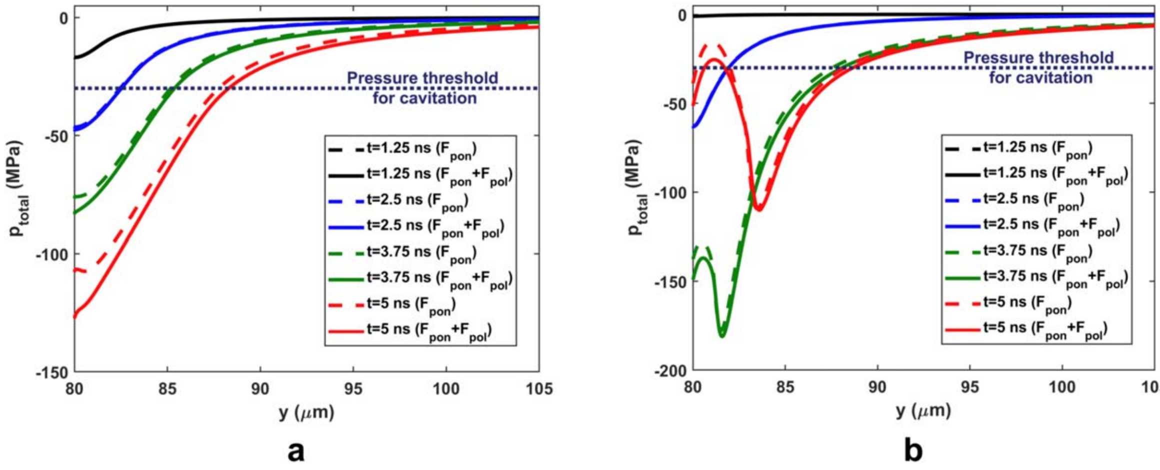

Figure 7. Center line distribution of total pressure at different time instances for (a) linear ramp and (b) pulse case. ($V_{\max} = 7.0\,\text{kV}$, $\beta = 1.0$.) The impact of polarization and ponderomotive forces on the total pressure is also shown. The dashed horizontal line represents the threshold pressure for cavitation of water.

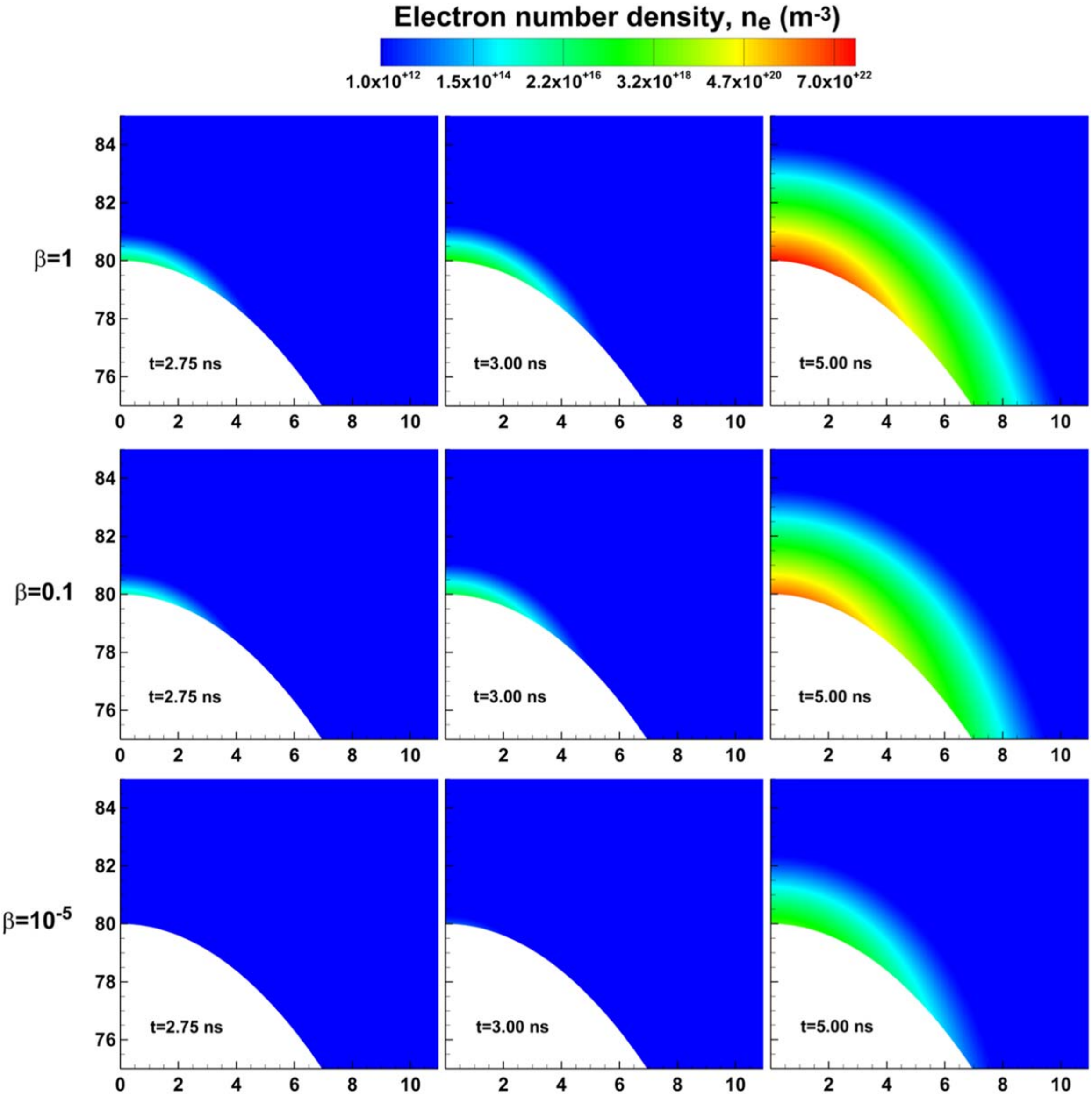

Figure 8. Spatio-temporal contour plots of electron number density for different values of fraction of ionizable species, β under linear ramp condition, $V_{\max} = 7$ kV.

For both the driving voltage profiles, the fluid density increases by ∼10%. However, the decrease in the density hence the degree of rarefaction is distinctively different between the two. In case of the pulsed voltage, the density decreases by ∼2% unlike the linear ramp where it does not even approach a percentage. In addition, a sharp gradient in the rarefaction is not observed under linear ramp condition rather the density decreases in a gradual fashion. The axial velocity evolution clearly shows that electrical forces drive the flow towards the electrodes. Under pulsed condition when the driving voltage starts to decrease an outward flow is established due to the formation of a high-pressure wave (figure 4(c)). For a maximum driving voltage of 7 kV the fluid velocity is found to remain in the subsonic regime.

To assess if the resulting pressure field is conducive of cavitation and possible rupture of the fluid, the evolution of the total pressure along the center line was analyzed. The center line profiles of p_{total} at different time instances are presented in figure 7. Simulations were also conducted with and without the inclusion of polarization forces to investigate the relative influence of polarization and ponderomotive forces. The predicted p_{total} for those conditions are also summarized in figure 7. The threshold pressure limit for water to rupture and cavitate is dependent upon a number of parameters, including the presence of dissolved gases, the degree of purity of the fluid, possible debris particles. Experiments [38] have demonstrated that at nominal ambient conditions (i.e. room temperature and atmospheric pressure) −0.15 MPa is sufficient to rupture the water under slower tension. However, under rapid stretching the threshold pressure limit increases significantly. The comprehensive experimental study of Herbert *et al* [39] reports that the threshold pressure limit for cavitation monotonically varies between −26 and −17 MPa for a temperature range of 0.1 °C–80 °C. Under

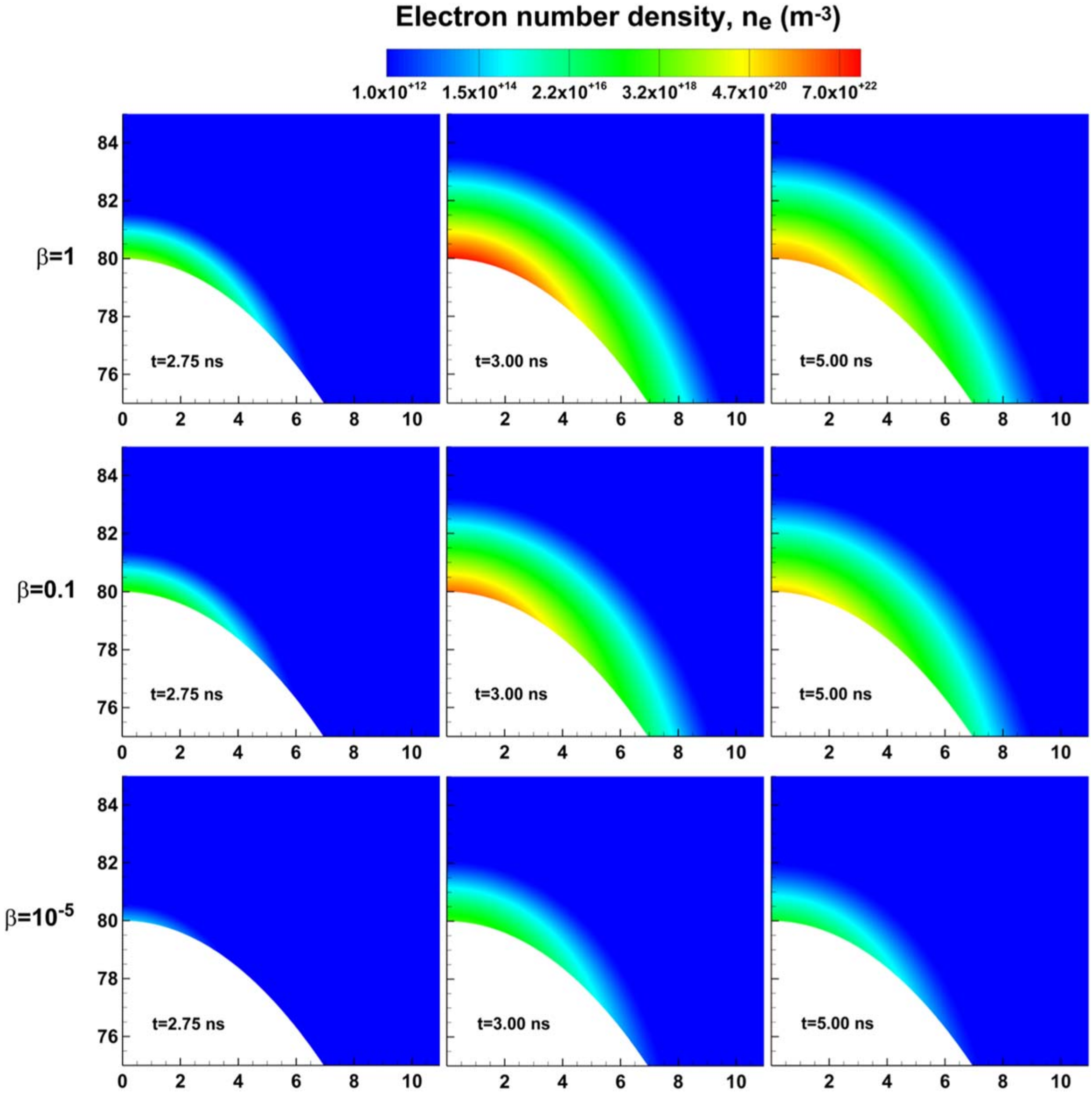

Figure 9. Spatio-temporal contour plots of electron number density for different values of fraction of ionizable species, β under pulsed condition, $V_{\max} = 7$ kV.

room temperature condition the threshold value was experimentally determined to be approximately −24 MPa. For our study, following Shneider and Pekker [24] we consider the threshold pressure limit for cavitation to be −30 MPa. The spatio-temporal evolution of p_{tot} clearly shows that for both voltage profiles when the maximum voltage is attained within 2.5–5 ns, conditions favorable for cavitation occur. However, for the linear ramp case (figure 7(a)) the threshold pressure condition is surpassed at 2.5 ns; before the maximum driving voltage condition (i.e. 5 ns figure 1(c)). Additionally, the negative pressure region is formed gradually and is observed to have lower spatial gradients. In contrast, the negative pressure region for the pulsed voltage has sharper gradients spatially with smaller region of influence. The comparison between the voltages suggest that the cavitation size is strongly dictated by the driving voltage profiles and nano voids can be formed with sharp voltage rise. The total pressure distribution further shows that the polarization force which has a slower response to change in electric field does not have an effect initially but becomes important later. Polarization force is directly dependent on the gradient of the dielectric permittivity and fluid density. As a result, its impact only becomes significant when a density gradient is established. Interestingly, it can be seen that due to the absence of polarization forces a pulsed voltage forms a stronger compressive pressure wave.

The evolution of electron number density, n_e for the two different voltage profiles are summarized in figures 8 and 9. The impact of β, fraction of ionizable species on n_e distribution is also shown. The β term denotes the fraction of neutral species that can undergo field dependent ionization i.e. ionization through Zener tunneling process. A higher β denotes that a higher fraction of the neutral species is available for field dependent ionization and vice versa. Since the

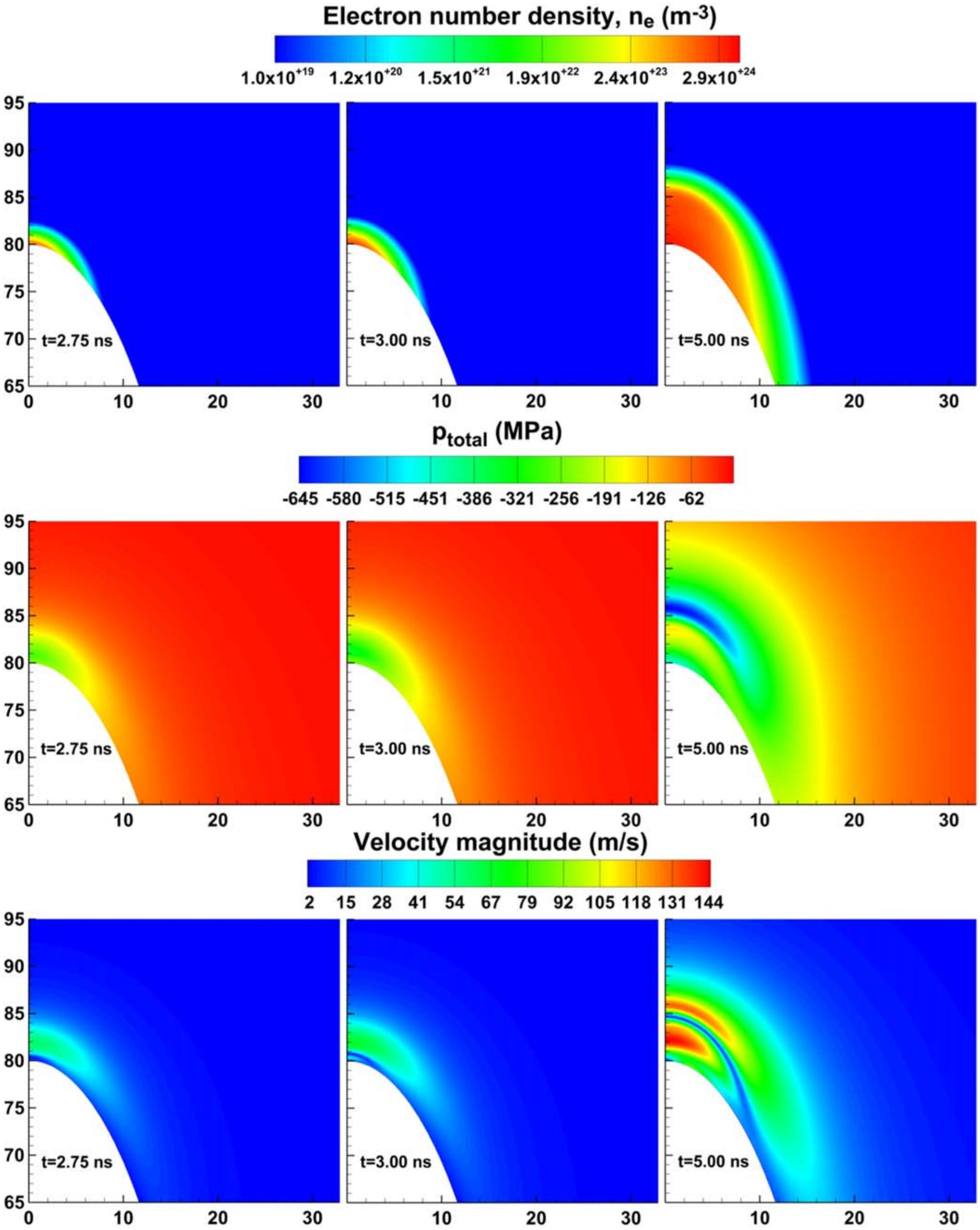

Figure 10. Spatio-temporal contour plots of electron number density, total pressure and velocity magnitude for a linearly increasing voltage $V_{\max} = 15\,\text{kV}$ and $\beta = 1$.

field dependent ionization is directly related to β, an increase in the β value results in higher electron number density. For both the voltage profiles the n_e are concentrated near the powered electrode. The peak n_e associated with $\beta = 1.0$ is found to be $2.2 \times 10^{23}\,\text{m}^{-3}$ and $1.5 \times 10^{23}\,\text{m}^{-3}$ for the pulsed and linearly ramped voltage profile respectively. The maximum ionization degree is $\sim 5 \times 10^{-6}$. The ionization is predominantly driven by field dependent ionization. As discussed by Kolb *et al* [40], due to the higher density of liquid, the scattering rates are high and mean free paths are low. As a result, the probability of mobile charges reaching ionization energy threshold is low unless a very high external electric field is introduced. However, the lack of strong lattice structure in liquids, allows ionization through Zener tunneling process possible at lower threshold values. For a peak voltage of 7 kV the electron impact ionization is insignificant due to low $|\mathbf{E}|/N$ values. The peak $|\mathbf{E}|/N$ (not shown here) remains around $\sim$22 Td and $\sim$25 Td respectively for the linear ramp and pulsed case. For the electron impact ionization channel to be effective, $|\mathbf{E}|/N$ values need to exceed $\sim$70 Td.

Simulations were also conducted with a higher maximum driving voltage to determine its impact on the overall characteristics of the system. For these cases the $V_{\max}$ was set at 15 kV with identical rise time and profiles as that of the 7 kV cases. The spatial contours of the electron number density, total pressure and velocity magnitude for the linear voltage ramp is presented in figure 10. It is evident that for a higher temporal gradient of the voltage (i.e. $3\,\text{kV ns}^{-1}$) a traveling

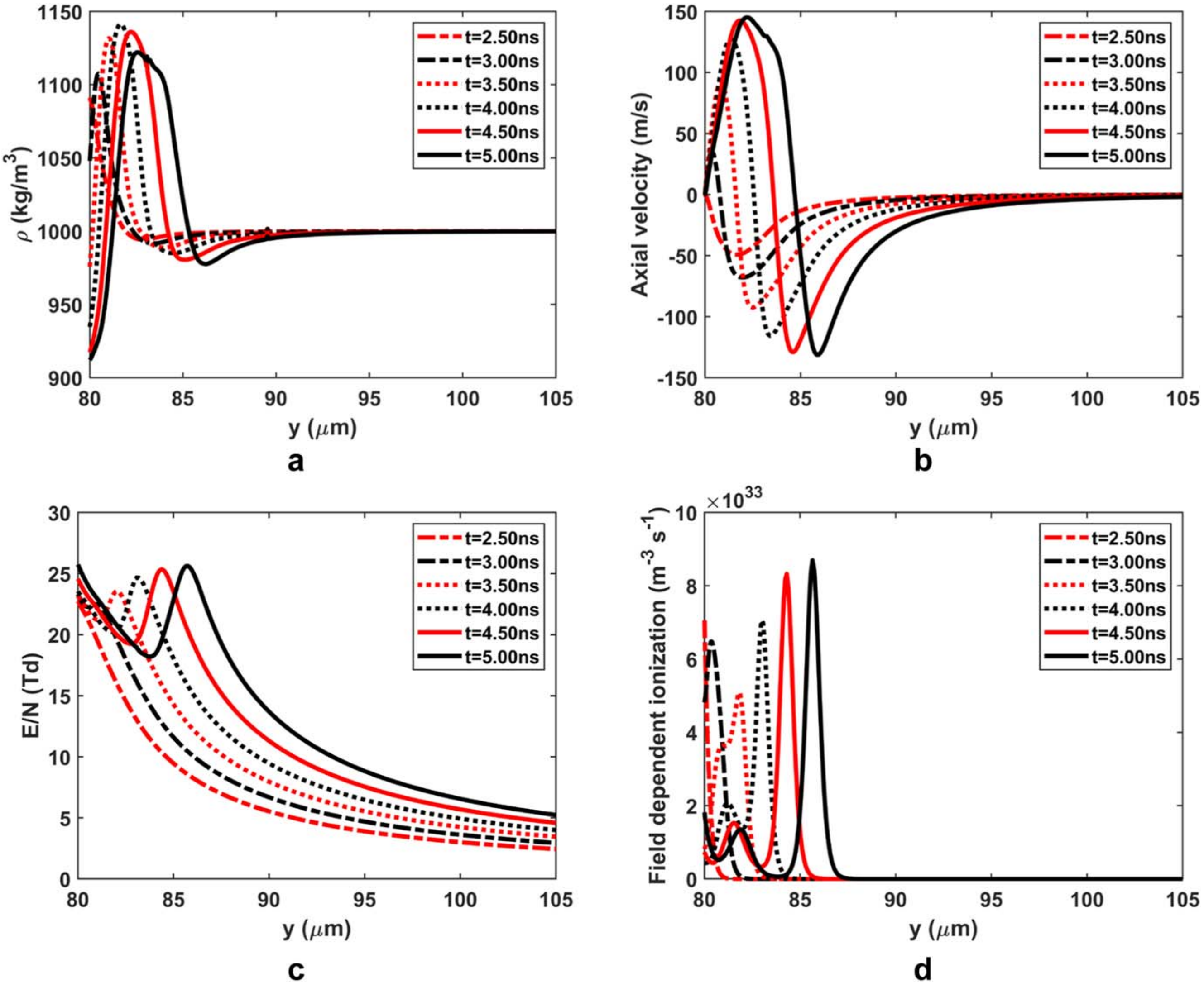

Figure 11. Temporal evolution of the center line (a) density, (b) axial velocity, (c) reduced electric field and (d) field dependent ionization for a linearly increasing voltage $V_{\max} = 15\,\mathrm{kV}$ and $\beta = 1$.

ionization and pressure wave is formed and the bulk fluid velocity is increased significantly. The velocity magnitude is observed to reach a maximum value of $\sim$145 m s^{-1} but still maintains subsonic conditions. The fluid velocity is directed towards the electrode till 2.50 ns after which there is a reversal in the flow direction (figure 11(b)). Unlike the 7 kV case where a compression in the total pressure is completely absent, for the 15 kV linear ramp a positive p_{total} is present. The lowest p_{total} is ~ -650 MPa which is well below the cavitation threshold limit and differs by a factor of $\sim$6 than that of the 7 kV case. The peak n_e is $\sim 4.0 \times 10^{24}\,\mathrm{m}^{-3}$ and the electron formation route is predominantly driven by the field dependent ionization (figure 11(d)). The field dependent ionization overlaps with the maximum reduced electric field location. The reduced electric field profiles suggest that under these conditions the electron impact ionization process still remains insignificant as the maximum $|\mathbf{E}|/N$ is $\sim$25 Td (figure 11(c)). The variation in the center line density profiles presented in figure 11 shows that the density undergoes sharp variations. The compression and expansion regions are initiated at 3.50 ns with a sub-micron low-density region near the electrode surface followed by a high-density region. The density increases and decreases by $\sim$15% and 8% respectively. The alternating low-high density region propagates further downstream at 5 ns and has a larger spatial influence. The decrease in $|\mathbf{E}|/N$ overlaps with the region of high density. Despite the formation of the low-density region the electric field across this region is not sufficient for electron impact ionization of water to be dominant. The ionization at this stage is still driven by field dependent ionization process.

The contour plots of electron number density, total pressure and velocity magnitude for the pulsed 15 kV voltage for identical time instances as the linear ramp is presented in figure 12. The peak n_e under pulsed condition is a factor of $\sim$6 higher than the linear case reaching a value of $\sim 2.4 \times 10^{25}\,\mathrm{m}^{-3}$. As the voltage rise time is further reduced in the exponential growth, the peak electron number density increases compared to the linear ramp and at the same time they are advected further downstream from the powered

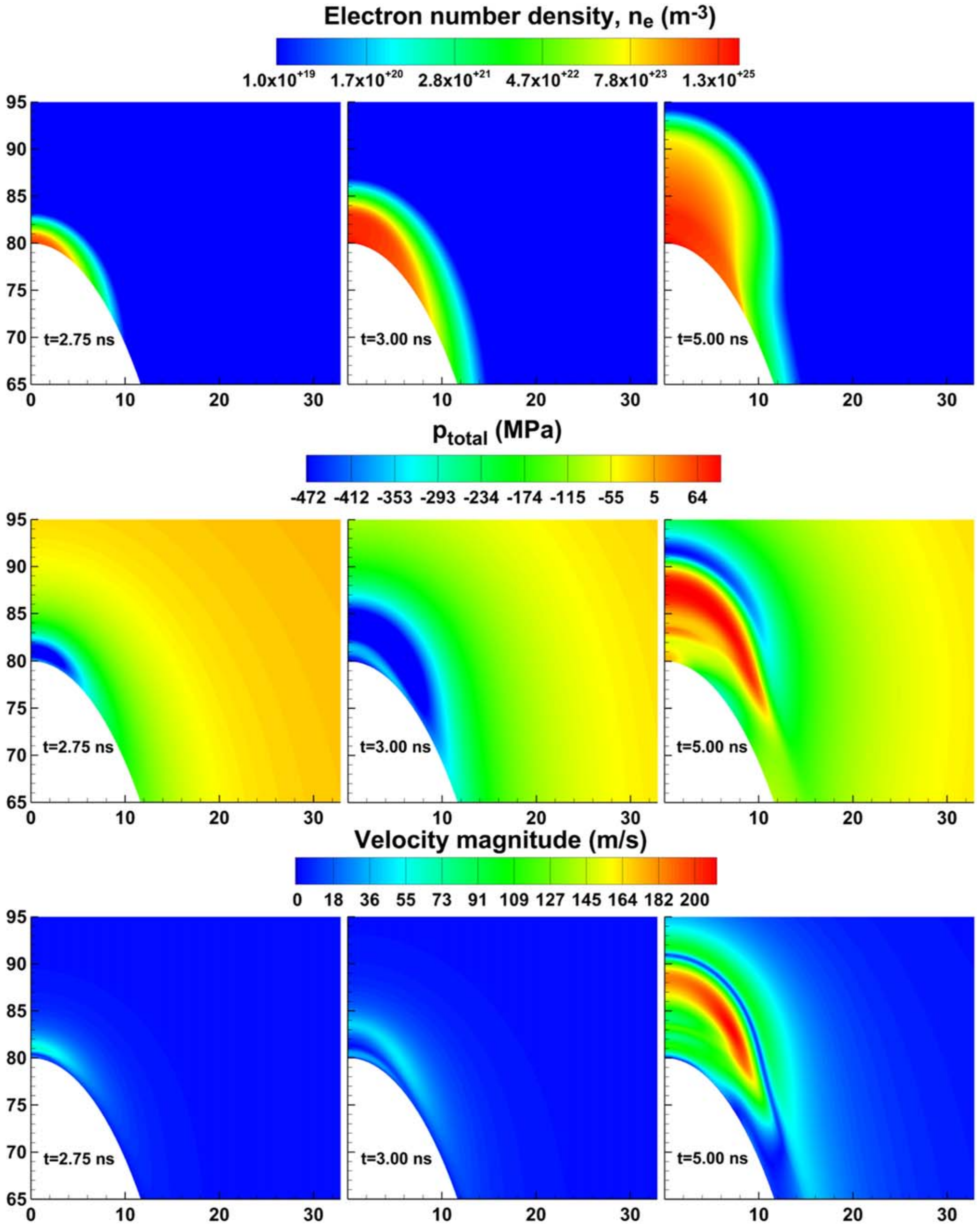

Figure 12. Spatio-temporal contour plots of electron number density, total pressure and velocity magnitude for a pulsed voltage $V_{\max} = 15$ kV and $\beta = 1$.

electrode. The downstream advection however takes place during the voltage relaxation (i.e. the linear decay in figure 1(c)). The bulk fluid velocity magnitude also reaches its peak value after the driving voltage starts to decrease due to the slower response of the liquid medium to electrical forces and the pressure variations. The predicted peak fluid velocity of $\sim$200 m s^{-1} is 12% of the peak electron drift velocity (e.g. v_d $\sim$1550 m s^{-1} for 30 Td) and is comparable to the negative and positive ion drift velocities. In comparison to the linear ramp of 15 kV, the exponential rise generates a stronger compressive wave in the total pressure distribution but at the same time forms a negative pressure that is well below the threshold cavitation pressure limit.

Figure 13 presents the center line distribution of density, axial velocity, reduced electric field and the field dependent ionization rate at different time instances for the pulsed voltage profile. The time instances are so chosen to show the temporal evolution right before the peak voltage, during the peak voltage and as the voltage starts decreasing. We can see that the decrease in the density happens before the peak voltage but is confined to a very small region near the electrode surface. The density variation propagates with the variation in the voltage and extends to $\sim$15 μm region along the centerline at 5 ns. In comparison to the linear ramp case, the density perturbation is lower. The bulk fluid velocity in general is found to travel away from the electrode in the low-

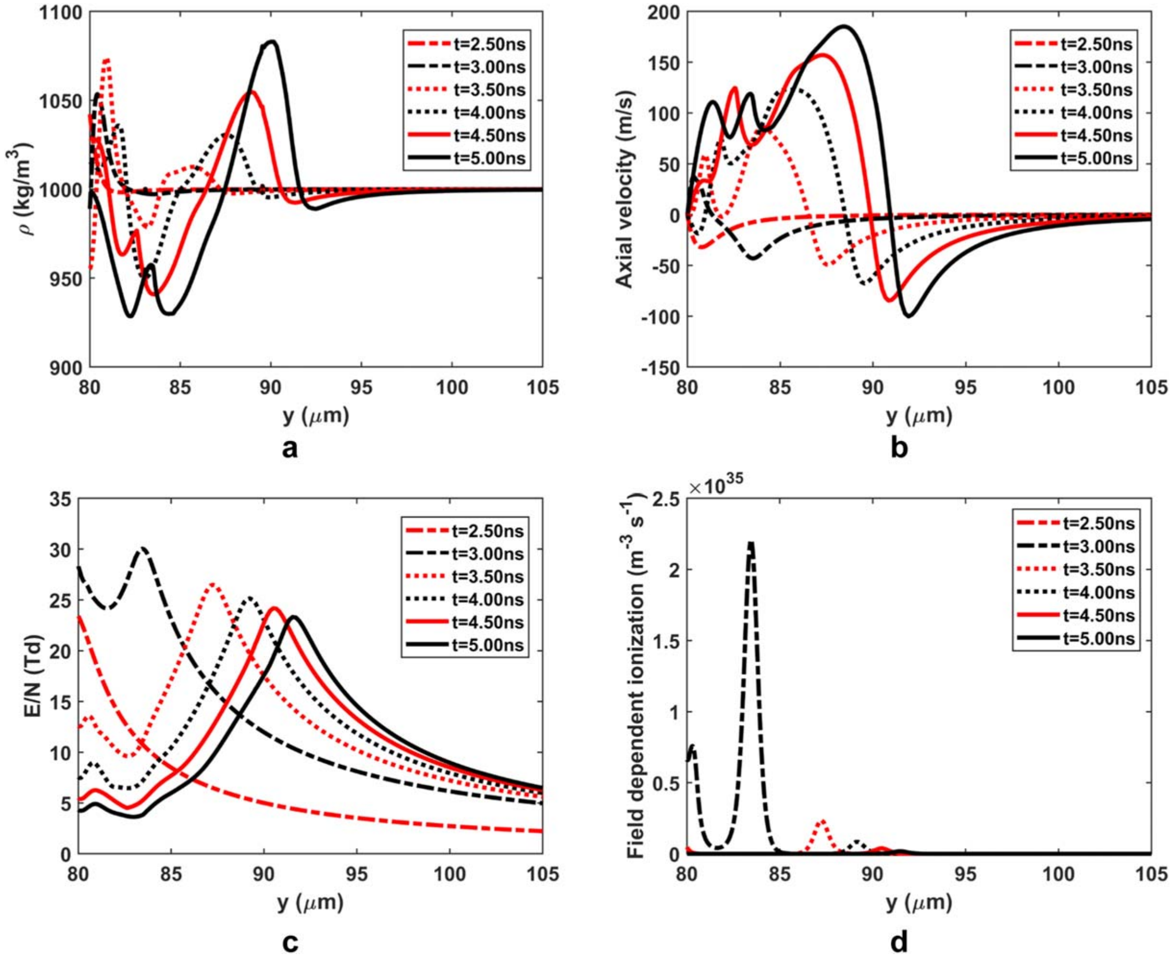

Figure 13. Temporal evolution of the center line (a) density, (b) axial velocity, (c) reduced electric field and (d) field dependent ionization for a pulsed voltage $V_{\max} = 15$ kV and $\beta = 1$.

density region and is directed towards the powered electrode when the density increases (figure 13(b)). The maximum reduced electric field $|\mathbf{E}|/N$ under a pulsed voltage is slightly higher (i.e. ~30 Td) but still not sufficient to allow significant electron impact ionization to occur. The ionization is dictated by the field dependent Zener tunneling and is an order of magnitude higher than the linear ramp case (figure 13(d)).

5. Conclusions

A multi-dimensional multi-physics model considering liquid phase compressibility has been developed to simulate the early stage of plasma initiation in a liquid medium and obtain insight on the coupled physicochemical process occurring during these extremely short time durations. The simulations were conducted for a powered needle-like electrode where the peak voltage and driving voltage profile was varied to assess its impact on the plasma initiation characteristics. The results show that the electrical body forces—electrostatic, polarization and electrostrictive ponderomotive, play a key role in generating strong density variation during the initial stage. Among the three electrical forces, electrostrictive ponderomotive force which is directly dependent on the gradient of the electric field has the strongest contribution. The polarization force only becomes effective when a density variation is established and in general has a slower response time. However, for a pulsed profile an earlier onset of strong polarization forces is observed resulting from fast and sharper variation in the fluid density. The model further shows that the fluid medium exposed to these electrical forces can easily reach cavitation threshold condition and forms a lower density region near the vicinity of the powered electrode. These low- density regions initiate on a sub-micron scale and then extends to a few microns during the course of complete voltage rise time.

Parametric study on the driving voltage profiles show that for an exponential voltage rise, the slow response of the fluid results in continuing variation in the fluid phase density and pressure during the voltage decay time. For a linear voltage rise (i.e. slower voltage rise), the resulting fluid velocity is directed towards the powered electrode which undergoes a reversal in direction as the voltage rise time is shortened via an exponential profile. The predicted peak electron number density ranges between $\sim 10^{23}$ and 10^{25} m^{-3} for the peak voltage values and profiles considered. The major electron formation route was found to be field dependent—Zener tunneling based ionization process even though possible low-density fluid region is formed due to cavitation like conditions. The electric field across the low-density region, due to the small spatial and temporal scales, do not reach conditions that allow electron impact ionizations to be significant and prominent. For higher values of peak driving voltages for both linear and exponential profiles the initial dynamics changes significantly. The fluid undergoes larger variation in density and the formation of stronger compression pressure waves are prevalent. The peak fluid velocity increases to hundreds of meters per second but still maintains subsonic conditions.

Acknowledgments

The work reported is supported by the Division of Physics of the US National Science Foundation under Grant No. 1707282.

ORCID iDs

Tanvir Farouk https://orcid.org/0000-0002-5579-0949

References

[1] Bruggeman P and Leys C 2009 Non-thermal plasmas in and in contact with liquids *J. Phys. D: Appl. Phys.* **42** 053001

[2] Locke B, Sato M, Sunka P, Hoffmann M and Chang J-S 2006 Electrohydraulic discharge and nonthermal plasma for water treatment *Ind. Eng. Chem. Res.* **45** 882–905

[3] Graham W G and Stalder K R 2011 Plasmas in liquids and some of their applications in nanoscience *J. Phys. D: Appl. Phys.* **44** 174037

[4] Bruggeman P J *et al* 2016 Plasma–liquid interactions: a review and roadmap *Plasma Sources Sci. Technol.* **25** 053002

[5] Locke B R and Thagard S M 2012 Analysis and review of chemical reactions and transport processes in pulsed electrical discharge plasma formed directly in liquid water *Plasma Chem. Plasma Process.* **32** 875–917

[6] Dawkin T and Berg D 1959 Luminous spots on electrodes in insulating oil gaps *Nature* **184** 120

[7] Gzowski O, Wlodarski R, Hesketh T and Lewis T 1966 The luminescence of dielectric liquids under high electric stress *Br. J. Appl. Phys.* **17** 1483–9

[8] Shammas N, Smith C and Calderwood J 1974 Coronas in insulating liquids *J. Phys. D: Appl. Phys.* **7** 2587–92

[9] Joshi R P and Thagard S M 2013 Streamer-like electrical discharges in water: part I. Fundamental mechanisms *Plasma Chem. Plasma Process.* **33** 1–15

[10] Tachibana K, Takekata Y, Mizumoto Y, Motomura H and Jinno M 2011 Analysis of a pulsed discharge within single bubbles in water under synchronized conditions *Plasma Sources Sci. Technol.* **20** 034005

[11] Tian W, Tachibana K and Kushner M J 2014 Plasmas sustained in bubbles in water: optical emission and excitation mechanisms *J. Phys. D: Appl. Phys.* **47** 055202

[12] Vanraes P and Bogaerts A 2018 Plasma physics of liquids-a focused review *Appl. Phys. Rev.* **5** 031103

[13] Bruggeman P J, Leys C A and Vierendeels J A 2006 Electrical breakdown of a bubble in a water-filled capillary *J. Appl. Phys.* **99** 116101

[14] Sommers B S and Foster J E 2014 Plasma formation in underwater gas bubbles *Plasma Sources Sci. Technol.* **23** 015020

[15] Babaeva N and Naidis G 2001 On streamer dynamics in dense media *J. Electrostat.* **53** 123–33

[16] Babaeva N and Kushner M J 2009 Structure of positive streamers inside gaseous bubbles immersed in liquids *J. Phys. D: Appl. Phys.* **42** 132003

[17] Levko D, Sharma A and Raja L 2016 Microwave plasmas generated in bubbles immeresed in liquids for hydrocarbon reforming *J. Phys. D: Appl. Phys.* **49** 22LT01-21-28

[18] Sharma A, Levko D, Raja L and Cha M 2016 Kinetics and dynamics of nanosecond streamer discharge in atmospheric pressure gas bubble suspended in distilled water under saturated vapor pressure conditions *J. Phys. D: Appl. Phys.* **49** 395205

[19] Joshi R, Qian J, Zhao G, Kolb J and Schoenbach K 2004 Are microbubbles necessary for the breakdown of liquid water subjected to a submicrosecond pulse? *J. Appl. Phys.* **96** 5129–39

[20] Lewis T J 2003 Breakdown initiating mechanisms at electrode surfaces in liquids *IEEE Trans. Dielectr. Electr. Insul.* **10** 948–55

[21] Lewis T J 1998 A new model for the primary process of electrical breakdown in liquids *IEEE Trans. Dielectr. Electr. Insul.* **5** 306–15

[22] Shneider M, Pekker M and Fridman A 2012 Theoretical study of initial stage of sub-nanosecond pulsed breakdown in liquid dielectrics *IEEE Trans. Dielectr. Electr. Insul.* **19** 1579–82

[23] Shneider M N and Pekker M 2013 Cavitation in dielectric fluid in inhomogeneous pulsed electric field *J. Appl. Phys.* **114** 214906

[24] Shneider M N and Pekker M 2013 Dielectric fluid in inhomogeneous pulsed electric field *Phys. Rev.* E **87** 043004

[25] Jacobs I S and Lawson A W 1952 An analysis of the pressure dependence of the dielectric constant of polar liquids *J. Chem. Phys.* **20** 1161–4

[26] Li Y-H 1967 Equation of state of water and sea water *J. Geophys. Res.* **72** 2665–78

[27] Shneider M and Pekker M 2016 *Liquid Dielectrics in an Inhomogeneous Pulsed Electric Field* (Bristol: IOP Publishing)

[28] Itikawa Y and Mason N 2005 Cross sections for electron collisions with water molecules *J. Phys. Chem. Ref. Data* **34** 1–22

[29] Hagelaar G J M and Pitchford L C 2005 Solving the Boltzmann equation to obtain electron transport coefficients and rate coefficients for fluid models *Plasma Sources Sci. Technol.* **14** 722–33

[30] Starikovskiy A, Yang Y, Cho Y and Fridman A 2011 Non-equilibrium plasma in liquid water: dynamics of generation and quenching *Plasma Sources Sci. Technol.* **20** 024003

[31] Qian J, Joshi R P, Schamiloglu E, Gaudet J, Woodworth J R and Lehr J 2006 Analysis of polarity effects in the electrical breakdown of liquids *J. Phys. D: Appl. Phys.* **39** 359–69

[32] Rothfuss C J, Medvedev V K and Stuve E M 2002 Temperature and field dependence of protonated water cluster emission from field adsorbed water layers on platinum *Surf. Sci.* **501** 169–81

[33] Rothfuss C J, Medvedev V K and Stuve E M 2003 The influence of the surface electric field on water ionization: a two step dissociative ionization and desorption mechanism

for water ion cluster emission from a platinum field emitter tip *J. Electroanal. Chem.* **554–555** 133–43

[34] Weller H G, Tabor G, Jasak H and Fureby C 1998 A tensorial approach to computational continuum mechanics using object-oriented techniques *Comput. Phys.* **12** 620–31

[35] Issa R I 1986 Solution of implicitly discretized fluid flow equations by operator splitting *J. Comput. Phys.* **62** 40–65

[36] Rhie C M and Chow W L 1983 Numerical study of the turbulent flow past an airfoil with trailing edge separation *AIAA J.* **21** 1525–35

[37] Geuzaine C and Remacle J 2009 Gmsh: a 3D finite element mesh generator with built-in pre and post-processing facilities *Int. J. Numer. Methods Eng.* **79** 1309–31

[38] Vinogradov V 2009 Depression of the cavitation centers in water under pulsed tension conditions *Tech. Phys. Lett.* **35** 54–6

[39] Herbert E, Balibar S and Caupin F 2006 Cavitation pressure in water *Phys. Rev.* E **74** 041603

[40] Kolb J F, Joshi R P, Xiao S and Schoenbach K H 2008 Streamers in water and other dielectric liquids *J. Phys. D: Appl. Phys.* **41** 234007